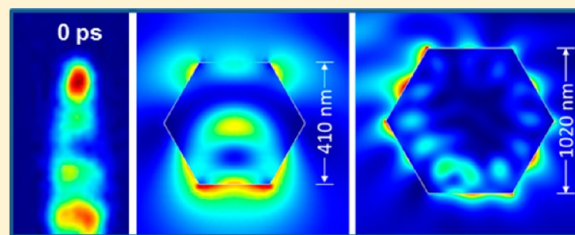


Pump–Probe Microscopy: Spatially Resolved Carrier Dynamics in ZnO Rods and the Influence of Optical Cavity Resonator Modes

Brian P. Mehl, Justin R. Kirschbrown, Michelle M. Gabriel, Ralph L. House, and John M. Papanikolas*

Department of Chemistry, Caudill Laboratories, University of North Carolina at Chapel Hill, Chapel Hill, North Carolina 27599-3290, United States

ABSTRACT: Femtosecond pump–probe microscopy is used to investigate the charge recombination dynamics at different points within a single needle-shaped ZnO rod. Recombination in the tips of the rod occurs through an excitonic or electron–hole plasma state, taking place on a picosecond time scale. Photoexcitation in the larger diameter sections of the interior exhibit dramatically slower recombination that occurs primarily through defects sites, i.e., trap mediated recombination. Transient absorption imaging shows that the spatial variation in the dynamics is also influenced by the cavity resonances supported within the hexagonal cross section of the rod. Finite element simulations suggest that these optical resonator modes produce qualitatively different intensity patterns in the two different locations. Near the end of the rod, the intensity pattern has significant standing-wave character, which leads to the creation of photoexcited carriers in the core of the structure. The larger diameter regions, on the other hand, exhibit intensity distributions in which the whispering gallery (WG) mode character dominates. At these locations, the photoexcited carriers are produced in subsurface depletion zone, where the internal fields separate the electrons and holes and lead to a greater degree of trap recombination on longer time scales.



1. INTRODUCTION

The finite sizes of individual particles introduce new dynamical phenomena not found in bulk materials. Quantum confinement of the carrier wave function occurs when the size is smaller than the exciton Bohr radius. It alters the electronic structure, resulting in tunable band gaps, tunable spectral properties, and dynamical phenomena that depend upon the size and shape.¹ Because the exciton Bohr radius is typically only a few nanometers, confinement is important in only the smallest structures, seemingly suggesting that size effects are unimportant beyond the nanoscale. Although different physical mechanisms are at play, larger structures also exhibit size and shape dependent phenomena. Surfaces and intrinsic defects trap mobile carriers resulting in internal electric fields that influence electronic structure and photophysical behavior.^{2,3} Band bending that arises from surface charging, for example, extends over tens to hundreds of nanometers and can separate photoexcited electrons and holes. In addition, optical resonator modes appear as the object dimensions approach the wavelength of light, impacting steady-state spectral properties and giving rise to nanostructure lasing.^{4–8}

This paper examines the electron–hole recombination dynamics in needle-shaped ZnO rods using femtosecond microscopy. Our results suggest that the resonator modes, in combination with internal fields, give rise to spatially variant carrier dynamics, revealing a connection between the shape and dynamical behavior present in larger mesoscale structures. ZnO is an excellent material for exploring the relationship between the structure and dynamics in this size range. The ability to manipulate the structure of ZnO is enormous, and through a variety of facile synthetic methods many different forms,

including nanorods with differing end morphologies, tetrapods, and nanohelices have been produced.^{9–11} The needle-shaped rods used in this study are 10–20 μm in length and have faceted hexagonal cross sections with diameters range from 1 to 3 μm at their widest point, down to 300–400 nm at the ends.

A key observation is that the carrier dynamics vary spatially along the structure, with the ends showing dramatically faster electron–hole recombination compared to the interior locations. Comparison of transient absorption and time-resolved emission measurements indicate that recombination at the ends of the structure occurs primarily across the band gap, through an excitonic or electron–hole plasma (EHP) state, whereas trap-mediated recombination dominates at the interior locations. This counterintuitive observation is the result of optical cavity modes supported by the hexagonal cross-section of the rod that result in different spatial distributions of the photoexcited carrier distribution at different points in the structure.

Cavity resonances become important when the size of the structure is comparable to the wavelength of light. The faceted crystalline structures of these ZnO materials give rise to a rich variety of optical cavity modes. Several groups have described longitudinal standing-wave modes propagating along the long axis of the rod.^{6–8} In addition to longitudinal modes, cavity resonances supported within the hexagonal cross-section of the

Special Issue: Paul F. Barbara Memorial Issue

Received: July 17, 2012

Revised: October 18, 2012

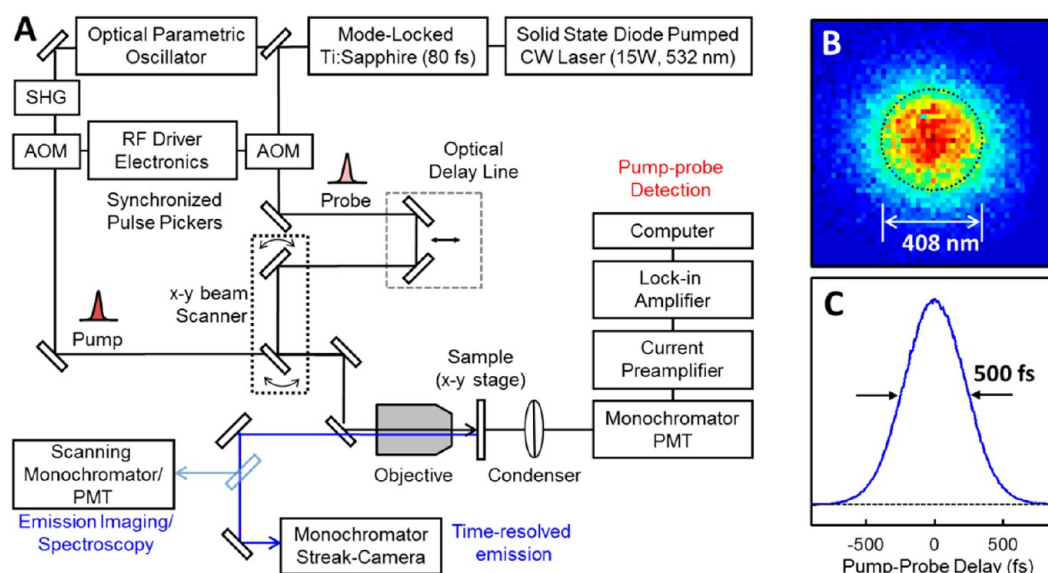


Figure 1. (A) Schematic diagram of a two-photon pump-probe microscope. The frequency-doubled output of an optical parametric oscillator (OPO) at 730 nm is directed on the back aperture of the microscope objective and focused to a diffraction-limited spot at the sample. Imaging is achieved by raster scanning the sample stage across the focused laser spot and monitoring the emission collected by the objective with a scanning monochromator/PMT. Pump-probe microscopy incorporates a second laser beam focused onto the location of the excitation beam. The beam that emerges from the sample is collected by a condenser lens, and its intensity is monitored by lock-in detection. Two acousto-optic modulators (AOM) are used to reduce the repetition rate of the laser to 1.6 MHz. Time-resolved emission measurements are performed by monitoring the emission intensity using a streak camera. (B) Two-photon emission image of a 100 nm nanoparticle with 810 nm excitation. The size of the emission feature suggests that the lateral resolution is approximately 410 nm. (C) Cross-correlation of the pump and probe pulses in the microscope obtained by monitoring the sum-frequency signal generated by the ZnO rod.

rod are also present. Previous reports describe these modes using two classic resonator pictures: Fabry–Pérot (FP) modes supported between two opposing parallel facets, and whispering gallery (WG) modes that correspond to the circulation of light around the periphery of rod via total internal reflection at each crystal face.^{12–19} For the experiments described here, where the excitation pulse propagates perpendicular to the rod axis, the transverse modes dominate the resonance effects.

The resonance conditions for both the FP and WG modes depend upon the diameter of the structure, and because of the tapered shape, a fixed excitation wavelength will go in and out of resonance as one moves along the long axis of the rod. We observed both types of resonances in second-harmonic and two-photon emission images,^{19–23} which appear as periodic intensity modulation along the long axis of the rod. Although the classic FP and WG resonator models^{12–19} reproduce, at least qualitatively, the image features, finite-difference frequency-domain (FDFD) calculations indicate these models are too simplistic. In this size regime (200–1000 nm diameter), the hexagonal resonator modes actually contain characteristics of both the FP and WG resonances, whose relative contributions vary with resonator size. At smaller sizes, the modes have primarily standing-wave character with much of the optical intensity located in the core of the structure. As the size is increased, the intensity distribution shifts to the periphery of the structure, becoming more WG-like in character.

We attribute the spatial variation in the recombination pathways (band-edge vs trap) to differences in these optical intensity distributions. The standing-wave modes existing at the ends of the rods create photoexcited carriers in the core of the structure, where they recombine through bulk-like mechanisms (e.g., exciton or electron–hole plasma recombination). In the larger cross sections, on the other hand, the WG mode distributions produce carriers in the space-charge region, and

the internal fields arising from the surface charge result in rapid charge separation and predominately trap-mediated recombination. These results point toward a connection between the shape of the object, and via its optical resonator modes, the charge carrier dynamics that follow photoexcitation.

2. EXPERIMENTAL SECTION

2.1. Materials. The ZnO rods were grown using hydrothermal methods adapted from previously published work.^{24,25} A 0.05 M reaction solution of $\text{Zn}(\text{NO}_3)_2$ and hexamethylenetetramine ($(\text{CH}_2)_6\text{N}_4$) is heated in a closed bomb, to yield needle-shaped rods ranging from 5 to 30 μm in length and from 0.3 to 2 μm in diameter. Size control is achieved by varying the reaction temperature, time, and/or concentration. After completion, the structures are harvested and sonicated in ethanol to break up aggregates and form a suspension. Microscopy samples are prepared by drop-casting $\sim 250 \mu\text{L}$ of the suspension onto a microscope slide with an etched reference grid. The grid facilitates the relocating of the rod for subsequent experiments in the optical microscope or structural characterization via SEM imaging. The ability to perform both optical and electron microscopy on the same structure allows us to correlate the photophysical observations with detailed structural information.

2.2. Imaging. The microscope combines an ultrafast laser source with a home-built far-field optical microscope for performing both two-photon emission imaging and time-resolved microscopy, in both pump-probe and emission configurations (Figure 1A). The femtosecond laser source consists of a mode-locked Ti:sapphire laser (810 nm, 80 fs, 80 MHz), whose output is split into two beams by an uncoated glass window. The more intense portion (96%) synchronously pumps a broad-band optical parametric oscillator (OPO),

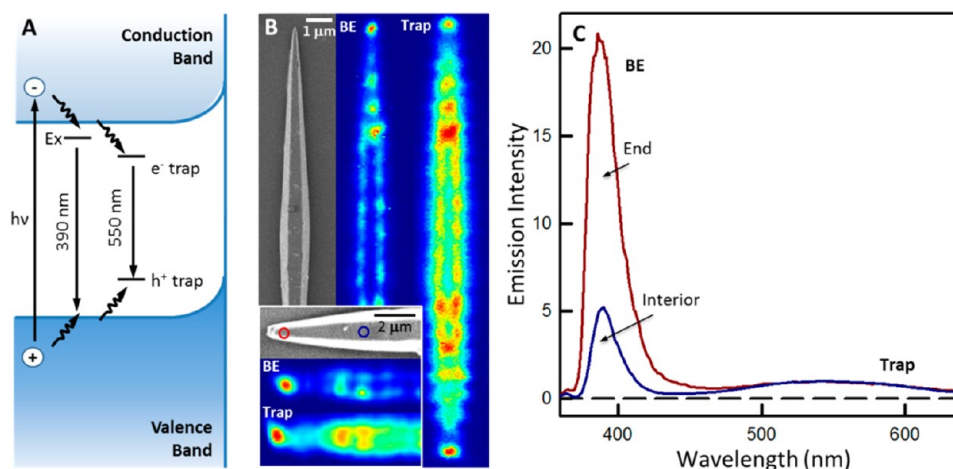


Figure 2. (A) Illustration of ZnO band structure depicting photoexcitation, band-edge emission at 390 nm from an exciton state (EX), and trap-mediated emission at 550 nm. (B) SEM and two-photon emission images (band-edge and trap) for two different structures. (C) Emission spectra observed at a point near the end and at a point within the interior of the rod are shown at the lower-left of panel B. Circles on the SEM image indicate locations of spectroscopic measurements.

whose frequency-doubled output at 730 nm (1 nJ/pulse) is used to excite the ZnO through a two-photon absorption process.

Conventional two-photon emission microscopy is achieved by directing the 730 nm beam onto the back aperture of a microscope objective (0.8 NA, 50 \times), which focuses it to a diffraction limited spot, resulting in two-photon excitation at a localized region of the ZnO rod. Light emanating from the structure is collected by the objective, passed through a dichroic beam splitter, and focused onto the slit of a monochromator and photomultiplier tube (PMT). Emission images are collected by raster scanning the sample across the focal point of the objective with a piezoelectric nanopositioning stage while monitoring the intensity of the emitted light. Imaging is performed without a cover slip under ambient conditions.

The spatial resolution of the microscope is determined by the size of the laser spot at the focus of the objective. Because two-photon absorption scales with the square of the optical intensity, efficient excitation occurs only at the focus, resulting in confocal-like behavior and a lateral excitation dimension that is smaller than the diffraction limit.²⁶ Emission images of a 100 nm particle (Figure 1B) indicate that the spatial extent of excitation is 380 nm for the 730 nm excitation, and 410 nm for 810 nm excitation. Both are slightly larger than the theoretical limits of 350 and 380 nm for the two different wavelengths, respectively.²⁶

2.3. Spatially-Resolved Spectroscopies. Spectroscopic observations are made at specific points within the structure by using the scanning stage to position the excitation beam. Emission spectra can be collected using a scanning monochromator. Time resolved photoluminescence measurements are performed with monochromator/streak camera. The streak camera separates the emitted photons in both wavelength and time and is capable of following the evolution of the emission spectrum with ≈ 15 ps time resolution.

2.4. Pump–Probe Microscopy. Transient absorption microscopy is achieved by combining the 730 nm excitation beam (pump pulse) with the weak reflection of the 810 nm mode-locked oscillator beam and then directing the copropagating pulse pair onto the back aperture of the microscope objective. Two synchronized acousto-optic modulator (AOM) pulse pickers reduce the repetition rates of the pump and probe

beams to 1.6 MHz, thus ensuring nearly complete relaxation before the next pump–probe pulse pair arrives.²⁰ A motorized linear stage controls the time delay between pump and probe pulses. Both the pump and probe pulses are focused to diffraction limited spots that are spatially overlapped within a single structure. The pump and probe polarizations were parallel to each other and oriented perpendicular to the long axis of the rod. The probe beam is collected by a condenser lens, focused onto the entrance slit of a monochromator, and detected by a photomultiplier tube and current preamplifier. The excitation beam is modulated at 4 kHz, and pump induced changes in the intensity of the probe pulse are monitored by a digital lock-in amplifier. The time resolution of the pump–probe measurement was characterized by cross-correlation of the two laser pulses using the frequency mixing properties of the ZnO (Figure 1C), which indicates a time-resolution of ~ 500 fs.

3. RESULTS AND DISCUSSION

Zinc oxide is a wide band gap semiconductor with a large exciton binding energy (60 meV). Photoexcitation by a single UV photon, or simultaneous two-photon excitation in the near-infrared, promotes electrons from the valence band to the conduction band. These free charge carriers (Figure 2A) can then either associate into excitons that lie just below the conduction band edge, resulting in a UV-blue emission at 390 nm or become trapped at defect sites in the crystal lattice, giving rise to a broad visible emission band centered at 550 nm.⁹

We have used a combination of two-photon emission and time-resolved microscopies to investigate the charge carrier dynamics at specific points within mesoscale ZnO structures. Two-photon emission images (section 3.1) reveal the presence of optical resonator modes. Transient absorption and time-resolved emission measurements (section 3.2) performed at different points within the same structure show that the charge carrier recombination is significantly faster at the ends of the structure, with the slower recombination in the interior regions being dominated by trap mediated pathways. Spatially separated pump–probe experiments (section 3.3) indicate that carrier diffusion out of the excitation volume is

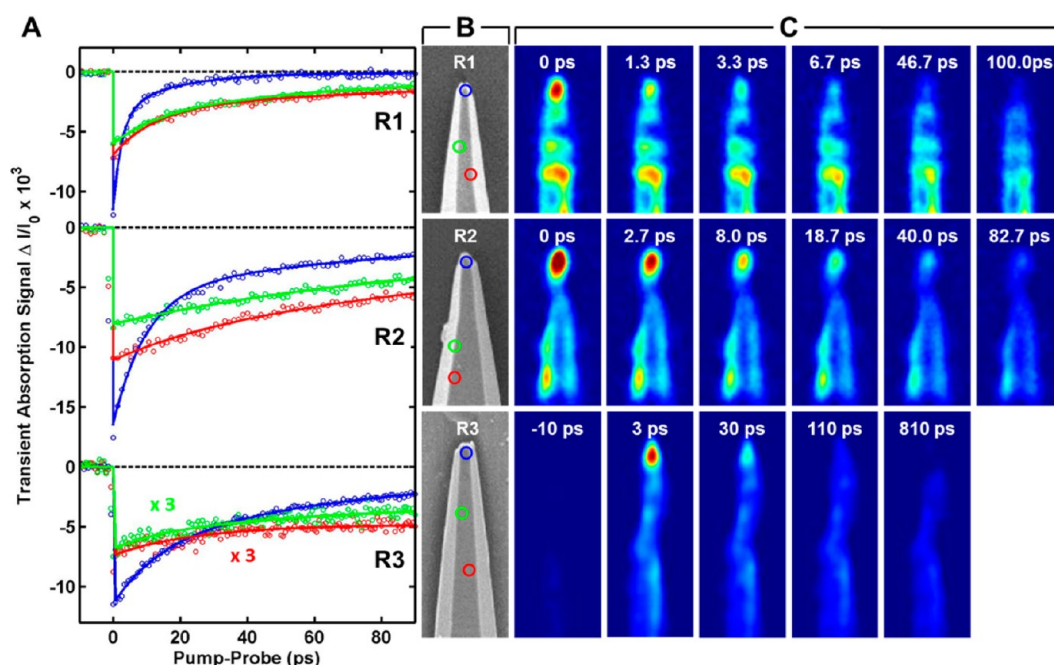


Figure 3. Pump–probe transients ($\Delta I/I_0$) collected from the end (blue) and two different points within the interior (green and red) from three different rods, R1, R2, and R3. The locations of the collected points for the three transients are indicated in the corresponding SEM images (B), where the horizontal dimension of each image is $3\ \mu\text{m}$. (C) Series of transient absorption images (ΔI) obtained at different pump–probe delays for the three rods. The series of pump–probe images show the rapid loss of the signal at the rod end, which ultimately decays to zero signal, whereas the response from the interior persists significantly longer.

insignificant, ruling out physical confinement and other mechanisms that require expansion of the charge cloud to explain the observed spatial variation. Finite-element simulations (section 3.4) suggest a connection between the spatially dependent dynamics and cavity resonator modes. They indicate that the WG modes, which are prevalent in the larger cross sections, produce carriers predominately in the surface depletion zone, where internal fields separate the electrons and holes, leading to greater trapping events and slower recombination.

3.1. Emission Imaging and Photoluminescence Spectroscopy. Scanning electron microscopy (SEM) and two-photon emission images acquired while monitoring the band-edge or the trap emission channels for two different rods are shown in Figures 2B. A prominent feature in many of the emission images is the variation in the emission intensity across the interior of the structure. Though the contrast varies from rod-to-rod, some structures exhibit a pronounced pattern of emission “spots” that are evenly spaced along the long axis of the rod. This intensity variation is a consequence of FP and WG modes supported within hexagonal cross section (Figure 2B). The tapered shape causes the fixed excitation wavelength to go in and out of resonance due to the changing diameter along the length of the rod, giving rise to the periodic emission pattern. Light couples more efficiently into the structure at the resonance locations, resulting in a greater number of photoexcited carriers, and hence a greater emission intensity.^{12,22,27}

Photoluminescence spectra (Figure 2C) obtained from the rod shown in the lower portion of Figure 2B show both the narrow exciton and broad trap emission bands that are characteristic of ZnO photoluminescence. The figure shows spectra collected following excitation at two different locations, indicated by the blue and red circles on the SEM image (Figure 2B, lower left). The relative intensities of the two emission

bands vary across the structure, with the end showing a more intense band-edge emission that suggests a greater propensity for e - h recombination across the band gap at that location.

3.2. Ultrafast Microscopy. Transient absorption microscopy with spatially overlapped pump and probe pulses were performed on three different rods denoted R1, R2, and R3 (Figure 3). The transient response (Figure 3A) was monitored at three different points in each rod, the end (blue) and two interior locations (green and red). The exact positions are indicated by colored circles on the corresponding SEM images (Figure 3B). The transients exhibit complex decay kinetics with fast ($<30\ \text{ps}$), intermediate (100 – $200\ \text{ps}$), and long ($>500\ \text{ps}$) components, whose relative amplitudes depend upon position. Interior locations exhibit all three components, with the fastest contributing only 25–50% of the total amplitude. On the other hand, the ends are dominated by the fastest component, which accounts for 60–100% of the amplitude.

Two different processes contribute to the magnitude of the pump–probe signals. The first is induced absorption, which arises from near-infrared excitation of free-carriers. In addition, there is a Kerr lens contribution, resulting from a spatial variation in the index of refraction associated with the localized photoexcited carrier distribution (vide infra). Although the absorptive component is negative, corresponding to a decrease in the probe beam intensity, the lensing contribution can result in either an increase or decrease in the probe intensity, and give rise to either a positive or a negative signal. Because the magnitudes of both the absorptive and lensing contributions depend upon the concentration of carriers, we attribute the decay of the pump–probe signal to the decrease in the free carrier population due to recombination and trapping events.

Pump–Probe Imaging. The carrier dynamics at the end of the rod differ dramatically from those observed at the interior, with the ends showing typically faster recombination rates than

any other point in the structure. Spatial variation is particularly apparent in images obtained by fixing the pump–probe delay and monitoring ΔI as a function of position (Figure 3C). At early delays, the largest signal is at the end of the rod. Although the overall signal in the interior regions is less intense compared to the end, there are localized, periodic regions of greater signal observed throughout the interior. This spatial modulation in the pump–probe signal is attributed to cavity modes (FP and WG modes) supported within the cross section of the structure.^{19,21,22} At longer delays, the bright spot at the end diminishes, becoming less intense than the interior and eventually disappearing altogether. Although differences from structure to structure are common in nanoscale materials, spatial variation in the dynamical response of individual objects has not been reported.

Combined Pump–Probe and Ultrafast Emission. Transient photoluminescence provides a direct view of the band-edge and trap mediated e–h recombination processes. A spectral-temporal intensity map (Figure 4A) of the time-resolved

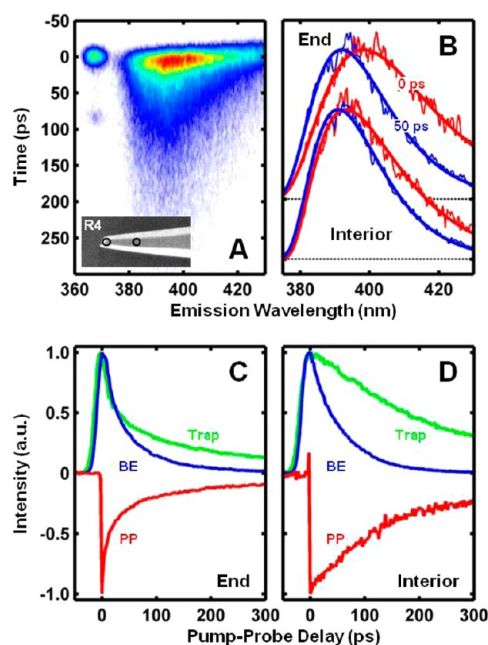


Figure 4. (A) Spectral-temporal intensity map of the emission collected from the end of the rod (R4) and detected using a streak camera. The main feature is the band-edge emission; the narrow peak at 365 nm is the second-harmonic of the excitation pulse and provides the instrument response (17 ps). The inset shows the SEM image and locations of spectroscopic measurements (end versus interior). The vertical dimension of the SEM image is 3 μm . (B) Time-resolved spectra obtained at 0 (red) and 50 ps (blue) from the end of the rod (upper set) and interior (lower set). (C, D) Comparison of the band-edge (BE), trap emission, and pump–probe (PP) data collected at the two points.

emission data collected from the end of a third rod, R3, shows a rich evolution of the band-edge emission, which shifts to the blue as it decays during the first 15–20 ps. Horizontal slices through the map correspond to snapshots of the emission spectrum at different times. The emission band initially appears with $\lambda_{\text{max}} \approx 400$ nm, and then narrows as it blue shifts to a limiting position of 390 nm.

Spectral shifts of this type are one signature of the electron–hole plasma (EHP) emission that occurs at high carrier

densities in II–VI semiconductors.^{28–30} When the carrier density exceeds the Mott threshold, Coulombic and exchange interactions weaken the exciton binding and reduce the band gap (i.e., band gap renormalization). This phenomenon gives rise to a collective EHP state with an intense, red-shifted emission relative to the exciton, as well as an enhanced recombination rate due to a greater degree of overlap between electron and hole wave functions. As electrons and holes recombine, the charge carrier density decreases, resulting in the time-dependent blue shift that reflects transition back to the excitonic state. Our time-resolved emission data indicate that the EHP to exciton transition in these structures occurs during the first 15–20 ps, consistent with observations in bulk and nanostructured ZnO.^{28,31} Photoexcitation of the interior shows a significantly smaller spectral shift (Figure 4B) and decreased propensity for EHP formation compared to the end. We estimate, on the basis of the two-photon cross-section,³² that $\sim 10^{20}$ carriers/ cm^3 are produced by the pump pulse. This is well above the EHP threshold reported for ZnO,³³ consistent with our observations.

A comparison of the pump–probe and photoluminescence decays (Figure 4C,D) shows qualitatively different behavior at the end of the rod compared to the interior. At the end of the rod, the decays of the pump–probe, band edge, and trap emission are similar to each other (Figure 4C), indicating that a major fraction of the electron–hole recombination events occur through the EHP state. At the interior location (Figure 4D), the pump–probe signal decays slowly, on the same time scale as the trap emission, suggestive of a carrier population that recombines primarily through defect states. These observations suggest that the overlap of the electron and hole wave functions persists in the tips of the rods, whereas at interior sites the two become spatially separated, suppressing band-edge recombination and resulting in a greater degree of trap mediated recombination. Given that the tips of the rods should possess the greatest concentration of defects, the conclusion that trap-mediated recombination is less important there is counter-intuitive.

The spatial variation in the dynamics could stem from several factors. A greater degree of physical confinement in the tips of the rod is one possible explanation. With no room for the charge cloud to expand in the narrow tips, the high carrier density formed upon photoexcitation persists, leading to a prolonged overlap of the electron and hole wave functions, and a propensity for EHP formation. In the interior of the structure, on the other hand, carriers can migrate away from the excitation region through simple diffusion, or perhaps driven by internal fields that separate the electrons and holes, resulting in a decrease in the charge density that makes it more difficult to form and sustain the EHP. Spatially separated pump–probe experiments (described below) probe the expansion of the charge cloud and test this hypothesis. A second possibility is that the spatial variation arises from a difference in *where* carriers are created (i.e., the core versus surface region). FDFD calculations are used to gain insight into distribution of the optical field within the structures. Overall, our analysis suggests that the spatial variation in the carrier dynamics arises not from carrier diffusion, but rather from different spatial distributions in where the charge carriers are created.

3.3. Spatially-Separated Pump–Probe Microscopy.

The spatially separated pump–probe configuration excites structures in one location and probes them in another by incorporating two separate positioning mechanisms for the

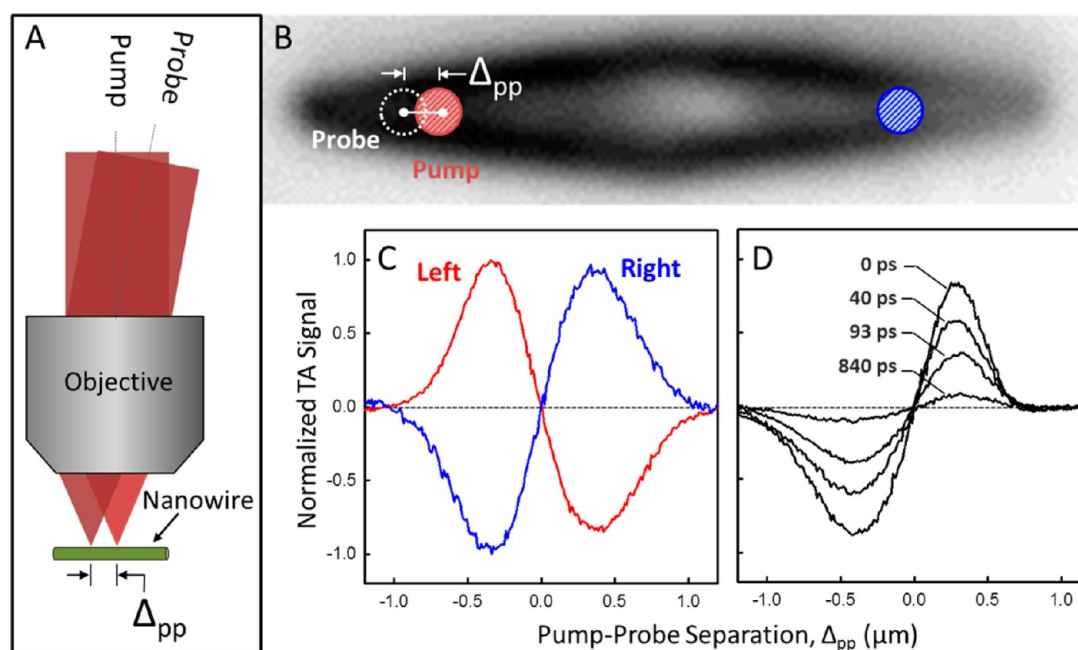


Figure 5. (A) Illustration of spatially separated pump–probe configuration via angle scanning of the probe beam. (B) Bright-field image of the ZnO rod showing locations of pump–probe separation scans. (C) Pump–probe signal as a function of the separation of the pump and probe spots at an early delay time. The red and blue scans correspond to data collected from the left and right locations, respectively. (D) Pump–probe separation scans obtained at a series of delays. Note: data in panels C and D were obtained from different rods.

pump and probe beams. One laser spot is positioned over a particular point in the structure via adjustment of the x – y sample stage. The position of the other beam is controlled by directing it through an x – y scanner that alters the angle it makes relative to the fixed beam as it enters the objective, causing it to be focused at point that is laterally separated from fixed beam by an amount Δ_{pp} (Figure 5A).

Contributions to Pump–Probe Signal. Figure 5 shows the transient absorption signal collected as a function of the separation between the pump and probe spots following excitation at two different locations within a single rod. These data were obtained with the probe beam fixed (scanned pump beam); however, similar observations are made with the pump beam fixed and probe beam scanned. Excitation toward either end of the rod results in derivative-like signals, with positive signals observed when the probe beam is placed between the pump spot and the rod tip. Because ZnO does not absorb in the near-infrared, the positive going signals cannot be the result of photobleaching. The derivative like signal results from interaction of the probe beam with the localized carrier distribution, resulting in a spatial variation in the index of refraction (i.e., a lens) that alters the direction of the probe beam as it passes through the rod. When the focused probe spot is positioned between the pump and the tip, it is deflected toward the middle of the rod. As the probe pulse exits the needle-shaped structure, it experiences a larger facet and greater clear aperture, and as a result, its intensity increases. When the probe is positioned on the other side of the pump spot, it is deflected toward the tip, experiences a smaller clear aperture and its intensity is reduced. Scans obtained at intermediate locations show that the negative lobe increases in magnitude as the pair is moved toward the center, becoming entirely negative at the midpoint (Figure 6). These results suggest that the pump–probe signals include contributions from both an induced absorption, arising from near-infrared excitation of

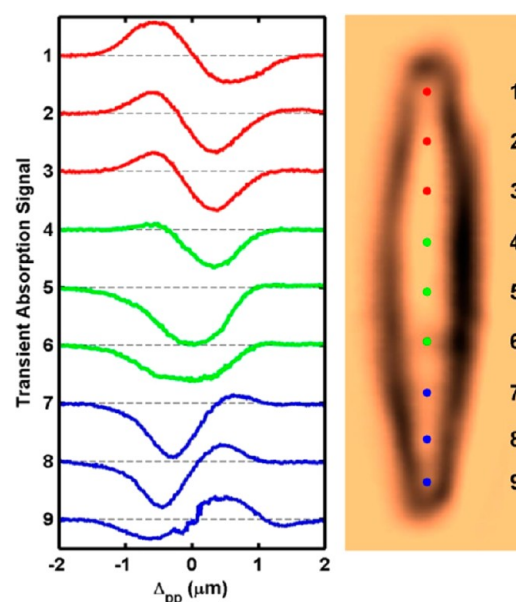


Figure 6. (Left) Transient absorption signal vs pump–probe separation (Δ_{pp}) at 1 ps pump–probe delay for nine different locations. (Right) Transmission image at 810 nm with nine different locations depicting positions of the Δ_{pp} scans along the c -axis.

free-carriers,³⁴ and a lensing component originating from a spatial variation in the index of refraction due to the localized excitation.^{32,35–37}

The transient lens created by photoexcitation could result from either a photoinduced electronic response (i.e., a Kerr lens) or local heating of the structure (i.e., a thermal lens). The relative magnitude of these two contributions can be estimated from the optical properties of ZnO. The Kerr lens results from intensity dependent, nonlinear polarization of the lattice due to optical excitation, and it includes both a nonresonant

contribution from the bound electrons and a resonant contribution from photoexcited charge carriers. The change in index of refraction of the ZnO due to the electronic excitation is given by^{32,38}

$$\Delta n^{\text{El}} = \gamma\Phi + \sigma_r N_{2hv} \quad (1)$$

where the first term corresponds to the instantaneous response of the bound electrons, whereas the second term arises from charge carriers produced through two-photon excitation. In this expression γ ($2.51 \times 10^{-11} \text{ cm}^2/\text{W}$ at 730 nm) is the bound-electron nonlinear refractive index, and σ_r ($3.02 \times 10^{-20} \text{ cm}^3$ at 730 nm) is the change in the index of refraction due to photoexcited charge-carriers, both of which have been measured using traditional Z-scan methods.³² N_{2hv} is the photoexcited charge carrier density produced by two-photon excitation, which we estimate, on the basis of the two-photon cross section,³² to be 10^{19} – 10^{21} carriers/cm³ under our experimental conditions. Pump–probe separation scans collected at a series of delays (Figure 5D) show that the lens persists at longer times indicating that the instantaneous response ($\gamma\Phi$) is a minor component of the overall signal, i.e., $\Delta n^{\text{El}} \approx \sigma_r N_{2hv}$. The thermal lens arises from local heating, which also alters the refractive index, i.e.

$$\Delta n^{\text{T}} = \frac{2E_{hv}}{\rho_0 C_p} \left(\frac{dn}{dT} \right) N_{2hv} \quad (2)$$

where C_p is the heat capacity ($40.17 \text{ J mol}^{-1} \text{ K}^{-1}$), ρ_0 is the density (0.069 mol/cm^3), and (dn/dT) is the thermal-optical coefficient ($0.7 \times 10^{-4} \text{ K}^{-1}$)³² for ZnO. The relative magnitude of the two effects is then

$$\frac{\Delta n^{\text{El}}}{\Delta n^{\text{T}}} = \frac{\rho_0 C_p \sigma_r}{2E_{hv} \left(\frac{dn}{dT} \right)} \quad (3)$$

Using known materials properties of ZnO suggests that the change in refractive index due to the electronic response is approximately 2000 times greater than the thermal affect, implying that the transient lens is the result of the photoexcited carrier distribution and not local heating.

This conclusion is further supported by the pump–probe separation profiles collected at a series of delay times. The shape of the profile is independent of delay, and its amplitude decay coincides with decay of the photoluminescence. If the lens were thermal in nature, the decay of the pump–probe separation profile would reflect the return of the lattice to its initial temperature, which would most likely not coincide with charge carrier recombination. This observation implies that the lens owes its origin to the photoexcited carrier distribution.

Carrier Diffusion. The pump–probe separation profile reflects the spatial extent of the carrier distribution, and the observation that it does not change as the carriers recombine suggests that there is not significant expansion of the initial charge cloud produced by localized excitation, at least on a length scale detectable with our spatial resolution. This further implies that physical confinement of the carriers is not the origin of the spatial variation observed in the charge carrier dynamics.

3.4. Role of Cavity Resonator Modes. The spatial variation observed in the pump–probe images is also observed in the band-edge and trap emission images.^{19–23} It is attributed to optical cavity modes supported by the rod's hexagonal cross section, which becomes visible when the structure's dimensions

are comparable to the wavelength of light. Both the FP and WG resonances have resonance conditions that depend upon the excitation wavelength and the cross-sectional diameter of the rod.^{12–19} Due to the needle shaped structure, the diameter changes along the length of the rod, causing the excitation light to go in and out of resonance, giving rise to the observed patterns.^{21,22}

We have used FDFD methods to simulate the distribution of the optical intensity within the structure.¹⁹ The simulation model (Figure 7A) consists of a Gaussian EM source that is

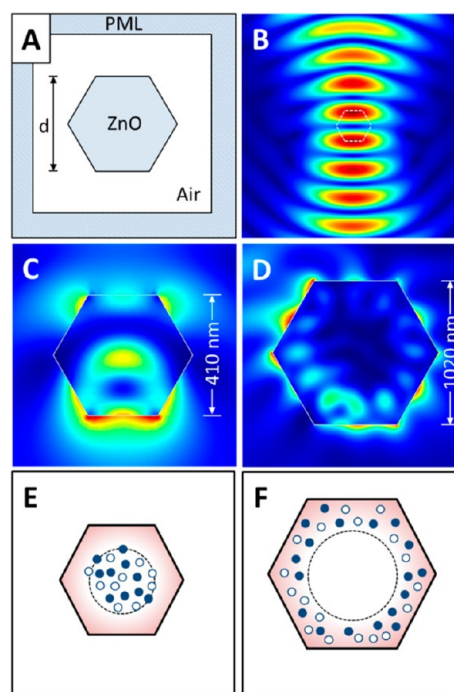


Figure 7. (A) Illustration of FDFD simulation cell. The two-dimensional model includes a hexagonal region representing the ZnO ($n = 2.2$), surrounded by air ($n = 1$). The EM source is placed at the top boundary and is parametrized to produce a focused spot at the center of box. The source is \vec{E} -field polarized parallel to the top boundary (i.e., perpendicular to the rod axis, which is normal to the page). (B) Magnitude of the optical electric field, $|\vec{E}|$, produced by the EM source in the absence of the ZnO rod. Red is maximum field and blue is zero field. The dashed hexagon in the center shows the size of a $d = 410 \text{ nm}$ resonator for reference. Distribution of the optical intensity (i.e., $|\vec{E}|^2$) for resonators with (C) $d = 410 \text{ nm}$, which is commensurate with the cross sectional diameter near the rod tip, and (D) $d = 1020 \text{ nm}$. For the smaller resonator, the EM source is centered over the top facet. For the larger resonator, the source is laterally displaced to the left of the resonator. Illustration of where carriers are created in the smaller (E) and larger (F) resonators.

focused onto a two-dimensional hexagonal slab of ZnO surrounded by air. The Gaussian source is placed at the boundary of the simulation box and is parametrized (i.e., frequency, numerical aperture, spatial extent at the boundary, etc.) to mimic the size and focus of the laser beam in the experimental arrangement and is polarized parallel to the top edge of the box. Figure 7B shows the optical field of the source in the absence of ZnO, with the hexagon depicting the cross-sectional size of the rod near the tip for comparison. The source is directed toward the ZnO from the top, and its center can be laterally offset relative to the center of the hexagonal slab. The

simulations suggest the intensity patterns in the tip differ from those observed in larger interior sections.

The maximum integrated intensity for larger resonator sizes, similar to the interior sections, occurs when the source is offset to one side or the other. These patterns have clear WG mode characteristics, with the largest intensity being located near the surface of the rod. This could be the origin of the increased trap recombination contribution observed in those regions. If the optical intensity is concentrated in the periphery of the rod, photoexcited carriers will be produced in the surface depletion zone (Figure 7F). The internal field present in this region (i.e., band bending) would separate the electrons and holes, resulting in a greater degree of carrier trapping and longer recombination times.

Near the tips of the rod, photoexcited carriers may be preferentially produced in the cores of the structure. This may simply result from a greater degree of scattering off the rough surfaces at the tip, resulting in a more spatially homogeneous intensity distribution. Another possibility suggested by the simulations is that for smaller resonator sizes, the intensity distribution has significant standing wave character, consistent with FP modes (Figure 7C), suggesting a greater density of photoexcited carriers will be produced in the core of the structure (Figure 7E). Regardless of the relative contributions of these two effects, both suggest that carriers in the tips will be produced in the central region of the rod. Because of the low carrier mobility, electrons and holes created in this zone would remain there, and experience a lattice environment similar to that of the bulk, accounting for the greater degree of recombination observed at the band edge.

Our experiments suggest that in this mesoscale size regime, light can couple into resonator modes, resulting in nonuniform excitation and spatially dependent dynamics. Although such modes have been discussed extensively,^{12–19} the role they play in shaping dynamical behavior has remained largely unexplored.

4. CONCLUSIONS

We have used femtosecond pump–probe microscopy to investigate the charge recombination dynamics at different points within a single needle-shaped ZnO rod. We find dramatically faster recombination in the tips of the rod that occurs through excitonic or electron–hole plasma states. Photoexcitation in the larger diameter sections of the interior exhibit much slower recombination, which proceeds primarily through defects sites, i.e., trap mediated recombination. Direct imaging of the excitation cloud using a spatially separated pump–probe method indicates that carrier diffusion in the excitation volume is not important in these experiments. Finite element simulations suggest that the spatial variation observed in the carrier recombination dynamics is the result of optical resonator modes, which produce qualitatively different intensity patterns in the two different locations. The intensity pattern near the end of the rod has significant standing-wave character, which leads to the creation of photoexcited carriers in the core of the structure. The larger diameter regions, on the other hand, exhibit intensity distributions in which the WG mode character dominates. At these locations, the photoexcited carriers are produced in subsurface depletion zones, where the internal fields separate the electrons and holes and lead to a greater degree of trap recombination on longer time scales. Although cavity resonator modes are known to alter steady-state optical properties, their impact on the carrier dynamics has not been extensively discussed.

AUTHOR INFORMATION

Corresponding Author

*Phone: (919) 962-1619. E-mail: John_Papanikolas@unc.edu.

Notes

The authors declare no competing financial interest.

ACKNOWLEDGMENTS

Funding for this project came from a grant from the National Science Foundation (CHE-0809045). The project also made use of instrumentation purchased by the UNC-EFRC Center for Solar Fuels, an Energy Frontier Research Center funded by the U.S. Department of Energy, Office of Science, Office of Basic Energy Sciences, under Award Number DE-SC0001011.

REFERENCES

- (1) Yoffe, A. D. *Adv. Phys.* **2002**, *51*, 799–890.
- (2) Allen, M. W.; Swartz, C. H.; Myers, T. H.; Veal, T. D.; McConville, C. F.; Durbin, S. M. *Phys. Rev. B* **2010**, *81*.
- (3) Tay, Y. Y.; Tan, T. T.; Boey, F.; Liang, M. H.; Ye, J.; Zhao, Y.; Norby, T.; Li, S. *Phys. Chem. Chem. Phys.* **2010**, *12*, 2373–2379.
- (4) Vanmaekelbergh, D.; van Vugt, L. K. *Nanoscale* **2011**, *3*, 2783–2800.
- (5) Yang, P. D.; Gargas, D. J.; Moore, M. C.; Ni, A.; Chang, S. W.; Zhang, Z. Y.; Chuang, S. L. *ACS Nano* **2010**, *4*, 3270–3276.
- (6) Ruhle, S.; van Vugt, L. K.; Li, H. Y.; Keizer, N. A.; Kuipers, L.; Vanmaekelbergh, D. *Nano Lett.* **2008**, *8*, 119–123.
- (7) Zimmler, M. A.; Bao, J.; Capasso, F.; Muller, S.; Ronning, C. *Appl. Phys. Lett.* **2008**, *93*, 051101–051104.
- (8) van Vugt, L. K.; Ruhle, S.; Ravindran, P.; Gerritsen, H. C.; Kuipers, L.; Vanmaekelbergh, D. *Phys. Rev. Lett.* **2006**, *97*, 147401–147405.
- (9) Ozgur, U.; Alivov, Y. I.; Liu, C.; Teke, A.; Reshchikov, M. A.; Dogan, S.; Avrutin, V.; Cho, S. J.; Morkoc, H. *J. Appl. Phys.* **2005**, *98*, 041301–041404.
- (10) Djuricic, A. B.; Leung, Y. H. *Small* **2006**, *2*, 944–961.
- (11) Wang, Z. L. *J. Phys.: Condens. Matter* **2004**, *16*, R829–R858.
- (12) Nobis, T.; Grundmann, M. *Phys. Rev. A* **2005**, *72*, 063806–063817.
- (13) Nobis, T.; Kaidashev, E. M.; Rahm, A.; Lorenz, M.; Grundmann, M. *Phys. Rev. Lett.* **2004**, *93*, 103903–103907.
- (14) Czekalla, C.; Nobis, T.; Rahm, A.; Cao, B. Q.; Zuniga-Perez, J.; Sturm, C.; Schmidt-Grund, R.; Lorenz, M.; Grundmann, M. *Phys. Status Solidi B* **2010**, *247*, 1282–1293.
- (15) Yang, Y. H.; Dong, J. W.; Wang, N. W.; Yang, G. W. *J. Appl. Phys.* **2011**, *109*, 093511–093517.
- (16) Yang, Y. H.; Zhang, Y.; Wang, N. W.; Wang, C. X.; Li, B. J.; Yang, G. W. *Nanoscale* **2011**, *3*, 592–597.
- (17) Liu, J. Z.; Lee, S.; Ahn, Y. H.; Park, J. Y.; Koh, K. H.; Park, K. H. *Appl. Phys. Lett.* **2008**, *92*, 263102–263105.
- (18) Sun, L. X.; Chen, Z. H.; Ren, Q. J.; Yu, K.; Bai, L. H.; Zhou, W. H.; Xiong, H.; Zhu, Z. Q.; Shen, X. C. *Phys. Rev. Lett.* **2008**, *100*, 156403–156407.
- (19) Kirschbrown, J. R.; House, R. L.; Mehl, B. P.; Gabriel, M. M.; Parker, J. K.; Papanikolas, J. M. *J. Phys. Chem. C* **2011**, manuscript in preparation.
- (20) House, R. L.; Mehl, B. P.; Kirschbrown, J. R.; Barnes, S. C.; Papanikolas, J. M. *J. Phys. Chem. C* **2011**, *115*, 10806–10816.
- (21) House, R. L.; Kirschbrown, J. R.; Mehl, B. P.; Gabriel, M. M.; Puccio, J. A.; Parker, J. K.; Papanikolas, J. M. *J. Phys. Chem. C* **2011**, *115*, 21436–21442.
- (22) Mehl, B. P.; House, R. L.; Uppal, A.; Reams, A. J.; Zhang, C.; Kirschbrown, J. R.; Papanikolas, J. M. *J. Phys. Chem. A* **2010**, *114*, 1241–1246.
- (23) Mehl, B. P.; Kirschbrown, J. R.; House, R. L.; Papanikolas, J. M. *J. Phys. Chem. Lett.* **2011**, *2*, 1777–1781.
- (24) Cheng, B.; Samulski, E. T. *Chem. Commun.* **2004**, 986–987.
- (25) Li, F.; Li, Z.; Jin, F. *J. Mater. Lett.* **2007**, *61*, 1876–1880.

- (26) Zipfel, W. R.; Williams, R. M.; Webb, W. W. *Nat. Biotechnol.* **2003**, *21*, 1368–1376.
- (27) Johnson, J. C.; Yan, H. Q.; Yang, P. D.; Saykally, R. J. *J. Phys. Chem. B* **2003**, *107*, 8816–8828.
- (28) Hendry, E.; Koeberg, M.; Bonn, M. *Phys. Rev. B* **2007**, *76*, 045214–045220.
- (29) Mitsubori, S.; Katayama, I.; Lee, S. H.; Yao, T.; Takeda, J. *J. Phys.: Condens. Matter* **2009**, *21*, 064211–064216.
- (30) Song, J. K.; Willer, U.; Szarko, J. M.; Leone, S. R.; Li, S.; Zhao, Y. *J. Phys. Chem. C* **2008**, *112*, 1679–1684.
- (31) Yamamoto, A.; Kido, T.; Goto, Y. F.; Chen, Y.; Yao, T.; Kasuya, A. *Appl. Phys. Lett.* **1999**, *75*, 469–471.
- (32) Lin, J. H.; Chen, Y. J.; Lin, H. Y.; Hsieh, W. F. *J. Appl. Phys.* **2005**, *97*, 033526–033532.
- (33) Klingshirn, C. F. *Semiconductor optics*, 3rd ed.; Springer: Berlin, New York, 2007.
- (34) Bauer, C.; Boschloo, G.; Mukhtar, E.; Hagfeldt, A. *Chem. Phys. Lett.* **2004**, *387*, 176–181.
- (35) Okamoto, K.; Fujita, S.; Kawakami, Y.; Scherer, A. *Phys. Status Solidi B* **2003**, *240*, 368–371.
- (36) Okamoto, K.; Inoue, K.; Kawakami, Y.; Fujita, S.; Terazima, M.; Tsujimura, A.; Kidoguchi, I. *Rev. Sci. Instrum.* **2003**, *74*, 575–577.
- (37) Okamoto, K.; Scherer, A.; Kawakami, Y. *Appl. Phys. Lett.* **2005**, *87*, 161104–161107.
- (38) Said, A. A.; Sheikbaha, M.; Hagan, D. J.; Wei, T. H.; Wang, J.; Young, J.; Vanstryland, E. W. *J. Opt. Soc. Am. B* **1992**, *9*, 405–414.